Available online at www.sciencedirect.com
SCIENCE DIRECT®
Estuarine, Coastal and Shelf Science 58 (2003) 541–554
ESTUARINE COASTAL AND SHELF SCIENCE

The influence of oceanic swell on flows over an estuarine intertidal mudflat in San Francisco Bay

S.A. Talke*, M.T. Stacey

Department of Civil and Environmental Engineering, University of California at Berkeley, Berkeley, CA 94720, USA

Received 3 May 2002; accepted 21 April 2003

Abstract

In this study, we examine the role that remotely forced ocean waves play in the hydrodynamics of an intertidal, estuarine mudflat. The observations indicate that long-period (10–20 s) ocean waves are a potentially important source of near-bed energy and shear stress in this environment. Over a two-week period in February 2001, we deployed an autonomous SonTek Hydra system on a mudflat in Central San Francisco Bay, and measured velocity and sediment concentration approximately 10 cm from the bed using an acoustic Doppler velocimeter (ADV) and an optical backscatter sensor (OBS). The experiment continued through wet (high tide) and dry (low tide) periods over an entire spring–neap cycle, and thus included the variation of near-bed velocity over a range of timescales. Results show that during large ebb tides, tidally forced flows dominate the near-bed dynamics during calm conditions. Wind waves dominate whenever the wind direction exposes the mudflat to wind coming off the bay (from the south and southwest), as occurs during winter storms. During periods when tidal forcing is limited and wind waves are small, remotely forced ocean swells become an important energy source. These motions appear in the burst samples at frequencies between 0.1 and 0.04 Hz and their energy correlates well ($\rho > 0.8$) with ocean swell measured from a buoy offshore of San Francisco. Spectral analysis of data shows that the average energy of ocean waves per tide varied between 2 and 15% of total energy load. Moreover, extreme values in the distribution of ocean waves bring episodic bursts of greater energy onto the estuarine mudflat, which may influence local suspension of sediments.

Keywords: mudflats; waves; currents; San Francisco Bay; shear stress

1. Introduction

Intertidal mudflats occupy an important niche in the estuarine environment, supporting an active food web and providing a transition zone and protective barrier between land and estuary (Dyer, 1998). Mudflats support large number of bivalves, crabs, worms, and microbiota, which feed either directly or indirectly on the productive microalgae in the sediments (Horne & Goldman, 1994). The habitat also provides a nursery ground for juvenile fish, and supports large numbers of shorebirds (Horne & Goldman, 1994). Due to its position between land and estuary, the intertidal zone also plays a crucial role in the transport of land-sourced sediments and contaminants into the estuary. Waves and currents interact to erode mudflats and vary with tidal range, seasons, and episodic events such as storms (Christie & Dyer, 1998). Sedimentation occurs during relatively calm periods, when accretion is higher than erosion (Christie & Dyer, 1998). Because they provide an extensive boundary condition, mudflats are an important component of the estuarine system, particularly with regard to sediments, contaminants, and organic matter (Dyer, 1989).

Hydrodynamically, the intertidal zone is influenced by processes with a wide range of timescales, from freshwater flow variations to diurnal and semi-diurnal tides to surface waves and turbulent mixing. When

* Corresponding author. Department of Civil and Environmental Engineering, 509 Davis Hall, University of California at Berkeley, Berkeley, CA 94720-1710, USA.
E-mail address: stalke@uclink.berkeley.edu (S.A. Talke).

0272-7714/03/$ - see front matter © 2003 Elsevier Ltd. All rights reserved.
doi:10.1016/S0272-7714(03)00132-X

considering either the biology of the mudflats or sediment and contaminant transport across them, the near-bed hydrodynamics, as defined by these forcing mechanisms, are critical. Energy dissipated from the boundary layers of waves and currents produces stresses at the bed (Grant & Madsen, 1979). Above a critical shear stress τ_{ce}, the bed erodes, while sediments settle out of the water column below a critical shear stress τ_{cd} (Krone, 1962; Partheniades, 1962). Wave action on cohesive sediments can fluidize the bed, which both dissipates wave energy and transports sediments (Li & Parchure, 1998; Wells & Kemp, 1986). Clearly, the energy dissipated from waves and currents form the mudflat environment; however, the hydrodynamic processes governing suspension of sediments are poorly understood at water depths less than 1 m (Christie & Dyer, 1998).

Depending on environmental conditions, either current (tidal or freshwater) or locally driven wind waves can dominate the suspension of sediments. On the Skeffling mudflat in the Humber estuary, bed shear stress and suspension are dominated by the mean flow (Christie & Dyer, 1998). At this mudflat, a threshold current ranging from ~15 to ~30 cm/s caused sediment concentration to increase above 20 mg/L at various locations (Widdows, Brinsley, & Elliott, 1998). By contrast, an intertidal mudflat at Portishead on the Severn estuary alternates between wind- and current-dominated conditions over a tidal cycle (Whitehouse & Michener, 1998). In their study, wave stirring increased suspended sediment concentrations by a factor of 3 during weak neap tides, but only by 10% during spring tides. At an intertidal mudflat in the Dutch Wadden Sea, accretion of sediments occurs during calm, current-dominated conditions. On the same mudflat, erosion occurs from a combination of tidal currents and wave action during rough conditions, while severe erosion occurs during stormy, wave-dominated conditions (Janssen-Stelder, 2000).

In addition to wind waves, longer frequency waves are important to the hydrodynamic and sediment transport processes of estuaries and mudflats. A cycle of offshore/onshore sediment transport can occur at infragravity frequencies due to correlation between sediment resuspension and intermittent wave groups (Green & MacDonald, 2001; Shi & Larsen, 1984). Storm surges, edge waves, and basin scale seiches accounted for approximately 5% of the wave energy in a shallow, mesotidal estuarine lagoon in New Zealand (De Lange & Healy, 1990). In that study, waves from the coastal ocean accounted for 70% of the total wave energy, even though most wave energy was filtered by the geometry of the harbor entrance and only high frequency components (3.5–4 s) entered (De Lange & Healy, 1990). Ocean waves are the principal forcing mechanism at a sandy intertidal flat at the mouth of an estuary in New Zealand (Green & MacDonald, 2001). However, the role of ocean swell in estuarine hydrodynamic processes is not often considered, particularly at sites well removed from the entrance to the estuary. In this paper, we consider the relative importance of ocean wave energy on an intertidal mudflat located approximately 12 km from the entrance to the San Francisco Bay. Though most ocean wave energy is dissipated before reaching intertidal mudflats, this study shows that it plays a small, but perhaps significant, role in the overall energy budget.

2. Materials and methods

The mudflat at the Richmond Field Station is located at 37°54′31″N, 122°20′0″W on the east side of San Francisco Bay, CA, near the cities of Berkeley and Richmond (Fig. 1a). Over the past 50 years, the mudflat has been greatly altered by human activity, perhaps most significantly by the former train tracks that now form its eastern boundary and by the remains of a breakwater that restrict the western exposure to the Central Bay (Fig. 1b). The mudflat is tidally forced and intertidal, with a tidal range of ~2.7 m. Two sub-tidal sloughs bisect the mudflat, and supply the adjacent marshland with tidal flow and drain seasonal runoff. Due to industrial activity in the past 100 years, the marsh is heavily contaminated with pollutants such as PCBs, mercury, and other heavy metals.

Our experimental setup consists of a lightweight aluminum frame (see Fig. 2) to which we attached an acoustic Doppler velocimeter (ADV), an optical backscatter sensor (OBS), and a conductivity–temperature (CT) probe. Data are logged to a 48 MB capacity storage unit in a watertight HYDRA module (from SonTek), which also provides power from an 18 V battery. For stability, the frame rests on two large, 4 square foot footpads; hollow structural beams are allowed to fill with water during a tide, adding weight and stability. Attached to the center of the frame (to ensure no interference from the side of frame), the ADV was focused ~10 cm from the bed, and it measured velocity in instrument coordinates. The OBS and CT probe were each mounted ~15 cm from the bed at the frame supports. The acoustic (from the ADV) and optical backscatter results are calibrated to sediment concentration by measuring the suspended sediments in a laboratory from samples during a high tide. The correlations between these data, and the implications for suspension, deposition, and transport of sediment will be a topic of future analysis; here, we focus on the time variability evident in the ADV velocity data.

We manually placed the experimental setup (see Fig. 2) on consolidated mud approximately 30 m from

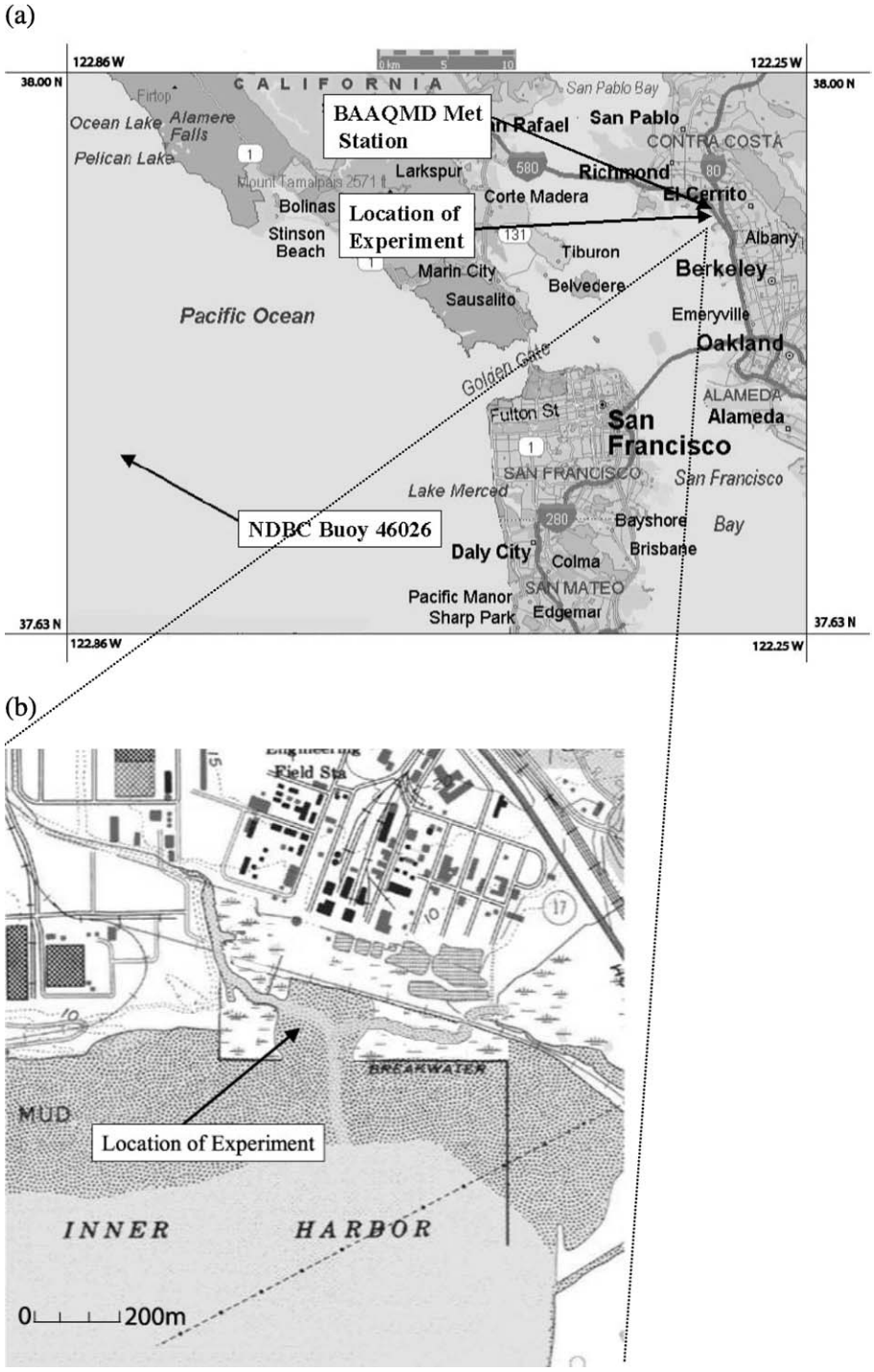

Fig. 1. Overview of the San Francisco Bay estuary (a) and location of the experimental site (b). Analysis made use of a meteorological station operated by the BAAQMD, located <1 km from the experimental site at the Richmond Field Station. In addition, we used data from buoy 46026, located to the west of San Francisco and operated by the National Data Buoy Center (NDBC). (a) is modified from the Microsoft Works Suite, while (b) is modified from the USGS map of the Richmond quadrangle.

the channel, which bisects the mudflat, and aligned the cross beam of the frame perpendicular to the dominant flow direction, as indicated by the bedform ripples (see Fig. 1b for experiment placement). Data were logged in bursts of 45 s at a rate of 10 Hz, and repeated every 5 min. Data were collected continuously, from 12:00 pm on February 2, 2001 to 11:00 am on February 15, 2001, capturing a total of 25 tidal cycles. Periods in which the instruments were submerged will be denoted as 'wet' periods, whereas periods in which the instruments were exposed to the air will be denoted as 'dry' periods.

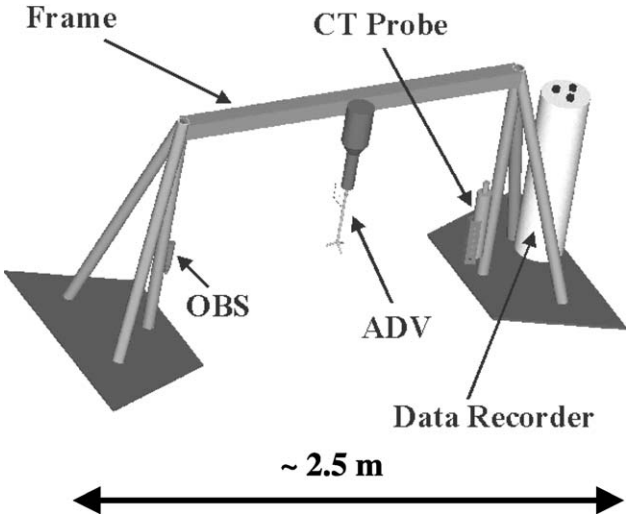

Fig. 2. Experimental apparatus. Note that the ADV was focused ~10 cm from the bed. The CT probe measured conductivity and temperature, and the OBS measured particle backscatter, at a height of ~15 cm. All data were logged to the data recorder. The length of the crossbar is approximately 1.3 m, and the height is approximately 1 m.

3. Results

In this paper, we will emphasize the frequencies of motions captured in the ADV velocity record, and determine which forcing mechanisms dominate the near-bed currents over the intertidal mudflat. Our results are divided into five sections. First, velocity data from the mudflat are shown and analyzed. Next, spectral data from an offshore buoy operated by the National Data Buoy Center (NDBC) near San Francisco (NDBC buoy 46026) are presented and correlated with the velocity data from the mudflat. Similarly, wind data from the Bay Area Air Quality Board (BAAQB) meteorological station at the Richmond Field Station are correlated with mudflat data. Next, we quantify some of the errors associated with the observations, which leads to a final section analyzing the bed stresses at the field location based on our water column observations. We discuss the implications of these results in the discussion that follows.

3.1. Results from acoustic Doppler velocimeter: velocity and frequency analyses

Both the amplitude and frequency of motion vary throughout the two-week experiment, and two distinct patterns of motion appear. This is illustrated by two contrasting 45-s bursts on February 3, 2001 (see Fig. 3a and b) and February 9, 2001 (see Fig. 3c and d). Logged at 6:10 am during a slack tide, the February 3 burst shows low-frequency (10–15 s period) oscillations around a small average velocity of about 1.5 cm/s. Transforming into frequency space using a fast Fourier transform (FFT), the maximum energy during this burst clearly occurs at 0.066 Hz, or a period of 15 s (see Fig. 3b). By contrast, larger-amplitude oscillations with a shorter period occur during the burst at 9:45 am on February 9 (Fig. 3c and d). In the frequency domain (Fig. 3d), it is clear that the energy during this burst occurs at the higher frequency of 0.35–0.6 Hz, corresponding to a period between 1.6 and 2.8 s.

The dominant frequency and amplitude evident in the 45-s bursts vary both over individual wet periods and on the longer timescales of days and weeks. In order to examine this longer timescale variability, we average the energy intensity of all bursts within each wet period, while preserving the frequency structure. That is, we define average energy intensity as

$$\overline{P(f,n)} = \frac{1}{T_n}\int_{t_1}^{t_2} P(f,t)\,\mathrm{d}t \tag{1}$$

where $P(f,t)$ is the energy intensity for each individual burst, and $\overline{P(f,n)}$ is the average energy intensity as a function of frequency, f, for each wet period n (of duration $T_n = t_2 - t_1$, the total time for which the instruments are submerged during a high tide). In other words, the spectra of Fig. 3b and d are averaged with other spectra from the same wet period. The results of averaging are shown in Fig. 4, which presents the energy intensity of the near-bed flows as a function of frequency (horizontal axis) and calendar day (vertical axis).

Two distinct energy bands are evident over the two weeks of the experiment, one between 0.05 and 0.1 Hz and another between 0.2 and 1 Hz (Fig. 4). The low-frequency band persists throughout the two weeks, with a maximum energy intensity of 0.04 and 0.02 $(\mathrm{m/s})^2/\mathrm{Hz}$ occurring on February 3 and 10, respectively, at a frequency of 0.667 Hz (period of 15 s). In between, less energetic motions occur at a frequency of 0.1 Hz, or a period of 10 s. The high-frequency band of energy primarily occurs between February 9 and 11, with a maximum occurring on February 11 at a frequency of 0.4 Hz and an intensity of 0.19 $(\mathrm{m/s})^2/\mathrm{Hz}$. Apart from this event, the extreme calm periods of February 3–4 and February 12 alternate with minor high-frequency signals from February 5 to 8 and from February 13 to 15.

While the tidally averaged energy intensity $\overline{P(f,n)}$ varies at the scale of days, the individual energy spectra found in the 45-s bursts vary on the timescale of minutes or hours. We can measure the variability by extracting the maximum energy intensity in each burst for both energy bands defined in Fig. 4, and plotting the results as a probability distribution. Fig. 5 shows the distribution of low-frequency energy (0.044–0.11 Hz; Fig. 5a) and high frequency energy (0.2–1 Hz; Fig. 5b) during the high tide on the morning of February 9. The energy intensity at low frequencies, corresponding to

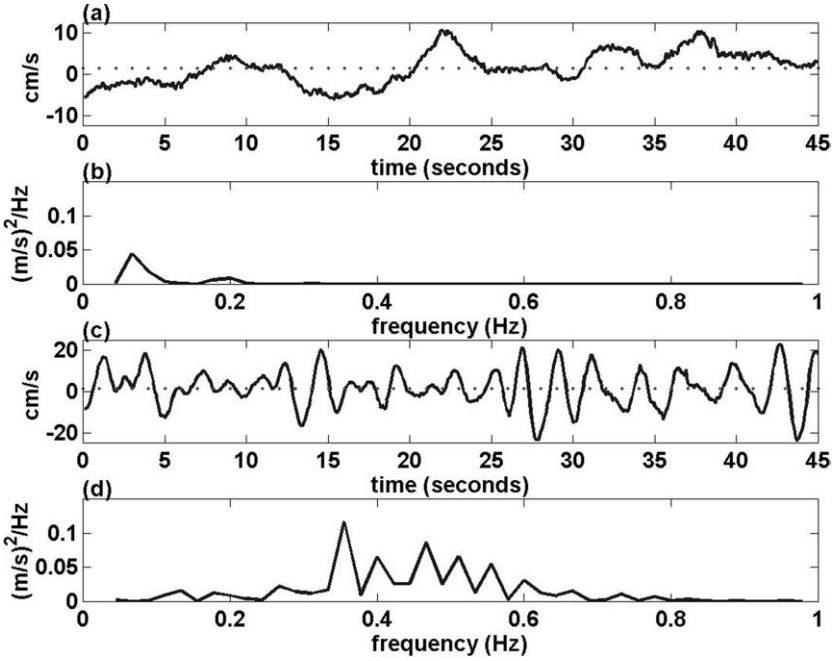

Fig. 3. Velocity time series and its FFT for a data set taken at 6:10 am on February 3, 2001 (a and b) and at 9:45 am on February 9, 2001 (c and d). Over the 45-s burst during a slack tide on February 3 (a), note that the spacing of peaks and troughs occurs at 5 and 15 s intervals in the velocity profile. This spacing is reflected in the maximum spectral density (b), which is $\sim$0.045 $(m/s)^2$/Hz at a frequency of 0.0667 Hz (i.e. a period of $\sim$15 s). A smaller peak occurs at a period of 5 s. The average current is small, with a value of 1.5 cm/s (see dotted line in (a)). Maximum velocity in (a) is 10.7 cm/s, while minimum velocity is $-$6.1 cm/s. Over the 45 s data set taken during a rising tide on February 9 (c), note that oscillating waves dominate over the average current, which is $\sim$1.6 cm/s. Note that the profile correlates with a period of high wind caused by a storm. Maximum energy is located between 0.35 and 0.6 Hz (d), with a maximum spectral density of $\sim$0.115 $(m/s)^2$/Hz occurring at a frequency of $\sim$0.35 Hz, corresponding to a wave of $\sim$2.8 s period.

wave periods between 9 and 22.5 s, is a well-defined distribution with a median energy density of $\sim$0.02 $(m/s)^2$/Hz (Fig. 5a). No discernable pattern of energy intensity is found in the higher frequency band (0.2–1 Hz), which is consistent with highly variable, locally generated wind waves (Fig. 5b). The maximum intensity of the higher frequency waves is an order of magnitude larger than the low-frequency waves—0.32 vs. 0.018 $(m/s)^2$/Hz. The low-frequency band's distribution closely resembles a Rayleigh distribution (Fig. 5a) with a mean value of 0.018 $(m/s)^2$/Hz. Frequently used to characterize the distribution of individual amplitudes of ocean waves, the Rayleigh distribution is given by (Longuet-Higgins, 1952)

$$f(a) = \frac{a}{\sigma^2}\, e^{-a^2/2\sigma^2} \qquad (2)$$

where $f(a)$ is the probability distribution of a wave of amplitude a and σ^2 is the variance of water surface height.

In Section 3.2, we explore the apparent coincidence between the distributions of ocean swell and spectral energy in the low-frequency band. Following that, we examine the intermittent high frequency band and its apparently random distribution of energy, noting that it was most energetic during the storm of February 9–11.

3.2. Ocean wave spectrum

The spectral peak of ocean swell on the Pacific Ocean typically is characterized by a period between 10 and 20 s, and swell amplitude is frequently described using a Rayleigh distribution. Thus, we hypothesize that the low-frequency band of energy on the intertidal mudflat is driven by surface waves from the Pacific Ocean. To establish that the low-frequency energy spectrum seen in Fig. 4 is coming from ocean waves, we obtained and plotted wave climate data for February 2001 from a buoy near San Francisco (NDBC buoy 46026, located at 37.75°N, 122.82°W (37°45′32″N, 122°50′00″W; see website http://seaboard.ndbc.noaa.gov/station_history.phtml?$station = 46026s for details). Fig. 6 shows the amplitude intensity from buoy 46026 as a function of frequency (horizontal axis) and calendar day (vertical axis). The characteristics of these spectra are qualitatively the same as those seen in the low-frequency band of the velocity record on the mudflat (see Fig. 4). For each graph (Figs. 4 and 6), a maximum amplitude occurs at frequencies between 0.05 and 0.1 Hz, or periods of 10–20 s. To be more specific, we see that the largest magnitude swells occur on February 3 and 10, and are characterized by a frequency of 0.067 Hz, or a 15 s period. In between, the waves shift to higher

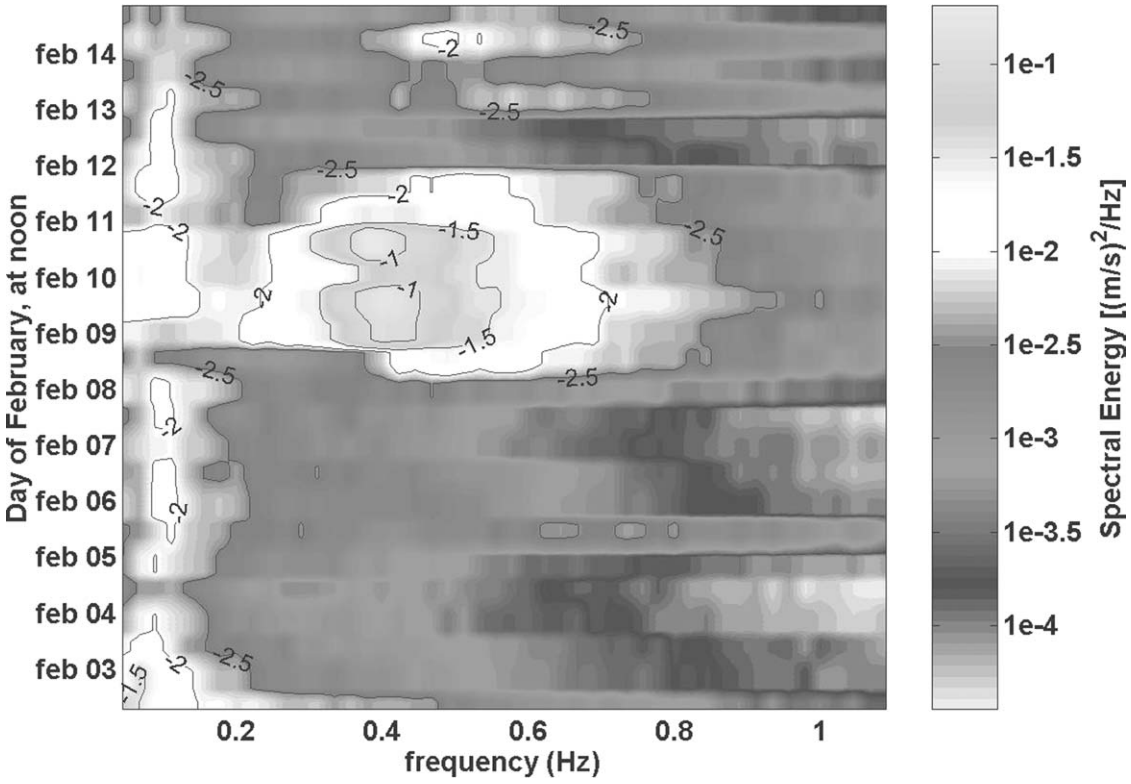

Fig. 4. Power spectrum obtained from ADV data at the mudflat, on a log 10 scale. Two distinct bands of energy can be seen, one between ~0.05 and ~0.1 Hz and another between ~0.2 and ~1 Hz. Contours on a log 10 scale mark energy domains from $10^{-2.5}$ to 10^{-1} $(m/s)^2/Hz$. Note that data between wet periods are interpolated.

frequency, but with smaller amplitude, with a period of about 10 s on February 6 and again on February 14. Comparison with Fig. 4 indicates that this is precisely the same behavior as was seen in the low-frequency band of the ADV velocity record.

More quantitatively, we calculate the correlation between the ocean buoy amplitude intensity and the mudflat energy intensity for motions at different frequencies. That is, we define correlation as (see a standard reference on statistical analysis for more detail, e.g. Shanmugan & Breiphol, 1998)

$$\rho_{PS}(f) = \frac{\frac{1}{M}\sum_{m=1}^{M}(\overline{P(f,m)} - \mu_P(f))(S(f,m) - \mu_S(f))}{\sigma_P \sigma_S} \tag{3}$$

where $\overline{P(f,m)}$ is the tidally averaged power spectrum (at frequency, f) spaced at hour long intervals m (see Eq. (1)), while data set $S(f,m)$ is the variation of the ocean spectral amplitude vs. time m (hours) and frequency f (Hz). Note that μ_P and μ_S are the time-averaged values of $\overline{P(f,m)}$ and $S(f,m)$ over the entire data set at each frequency f, respectively, while σ_P and σ_S are the standard deviations of $\overline{P(f,m)}$ and $S(f,m)$ at each frequency f, respectively. The total length of the data set is given by M, and denotes the number of hours in the experiment. The variation of $\rho_{PS}(f)$ with frequency is shown in Fig. 7, and confirms the qualitative agreement observed between the ocean swell energy and the mudflat motions. At a period of 15 s, the correlation coefficient is greater than $\rho = 0.8$, while the correlation over the range of ocean swell (0.05–0.1 Hz) is greater than $\rho = 0.7$.

From this analysis, we conclude that the low-frequency (periods of 10–20 s) wave motions evident on the intertidal mudflat are driven by swells on the Pacific Ocean. As such, wave motions will be evident in the intertidal zone, even when local wind forcing (as will be considered in the next section) is small. During periods of energetic ocean swells but less energetic local winds, we would expect this contribution to the dynamics of the mudflat to be significant.

3.3. Wind energy

The high-frequency band of energy on the intertidal mudflat is most energetic during a storm (on February 9–11) containing significant wind energy, suggesting that local winds drive these motions. Wind data were obtained from the Bay Area Air Quality Management District (BAAQMD, Meteorological Tower number 2950; D. Duker, personal communication) located at the Richmond Field Station (<1 km from the experimental site). Because of the breakwater, the mudflat is

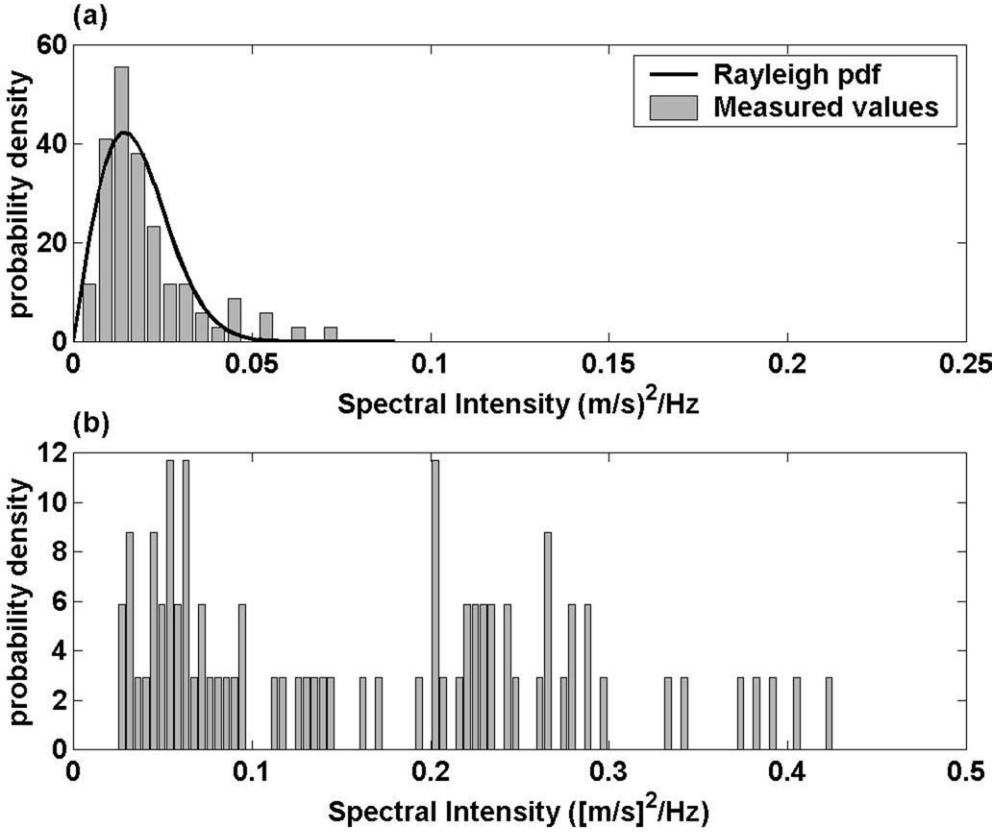

Fig. 5. Comparison of the probability density distribution (pdf) of the maximum spectral intensity found between 0.044 and 0.11 Hz (a) and between 0.2 and 1 Hz (b) for a wet period occurring between 10:40 pm on February 9, 2001 and 4:55 am on February 10, 2001. Note that the low-frequency pdf (a) resembles the Rayleigh distribution typically found in distributions of ocean waves. On the other hand, the pdf of the higher frequency band (b) is less structured, indicating a quickly changing wave climate.

only exposed to significant fetch for winds directed from the south or southwest (see Fig. 1). To account for this, we have conditioned our wind forcing to be non-zero only when the orientation of the wind is between 165° and 225° east of true north. In Fig. 8a, the conditioned wind forcing is illustrated in a vector format, with calendar day on the vertical axis and time of day on the horizontal. The time variability of the magnitude of this forcing is shown in Fig. 8b, and qualitatively depicts the same variability as the high-frequency band of Fig. 4. A large peak in wind forcing is evident between February 9 and 11, with smaller events occurring on February 5 and 14.

To quantify the relationship between local wind forcing and the high frequency motions on the mudflat (see Fig. 4), we define a correlation between wind energy (defined as the conditioned wind magnitude squared) and near-bed energy intensity at each resolved frequency, using a modified version of Eq. (3). In place of $S(f,m)$ (ocean swell amplitude spectrum), μ_S (time-averaged amplitude), and σ_S (standard deviation of $S(f,m)$, we use the conditioned wind energy, $E_w(m)$, which is a function of the time increment m (hours), the time-averaged wind energy μ_E, and the standard deviation of wind energy σ_E.

Using the conditioned wind data, we find that most correlation values at frequencies between 0.2 and 1 Hz are substantially greater than $\rho = 0.6$ (see Fig. 9) and that between 0.25 and 0.8 Hz, correlation is greater than $\rho = 0.7$. We conclude that the high-frequency waves, with periods between 1 and 5 s, are driven by local winds on the estuary coming from the south and southwest.

3.4. Discussion of error

The ADV reports an error of less than 2 mm/s per measurement (SonTek, 2001) when sampling at a frequency of 10 Hz with a velocity range of 30 cm/s. Using standard error propagation techniques, this results in an error in the total energy (velocity squared) of 0.0002 (m/s)^2, assuming an average velocity of 5 cm/s (Bendat & Piersol, 1966). However, because we are averaging our results over a tidal period with typically more than 50 bursts, our error is reduced by a factor of more than 7, resulting in a conservative error estimate of less than 5×10^{-5} (m/s)^2. The energy detected in the power spectrum is above the calculated error level, ranging from $\sim 10^{-4}$ to $\sim 10^{-3}$ (m/s)^2 for the low-frequency band

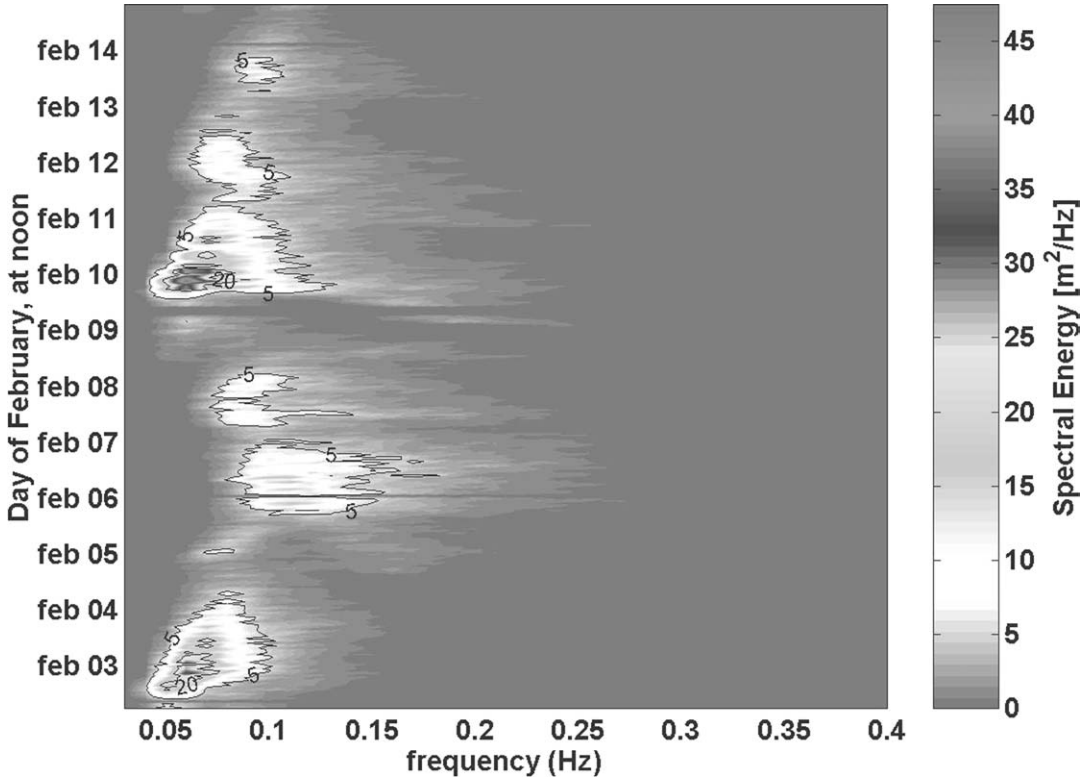

Fig. 6. Wave amplitude spectrum from NDBC buoy 46026, located just offshore of San Francisco, from February 2 to 15, 2001. Note the shift in the maximum wave period from approximately 15 s on February 3 to approximately 8–10 s on February 6. Contours mark amplitude intensities of 5 and 20 m^2/Hz. The maximum amplitude intensity of 47.5 m^2/Hz occurs on February 10.

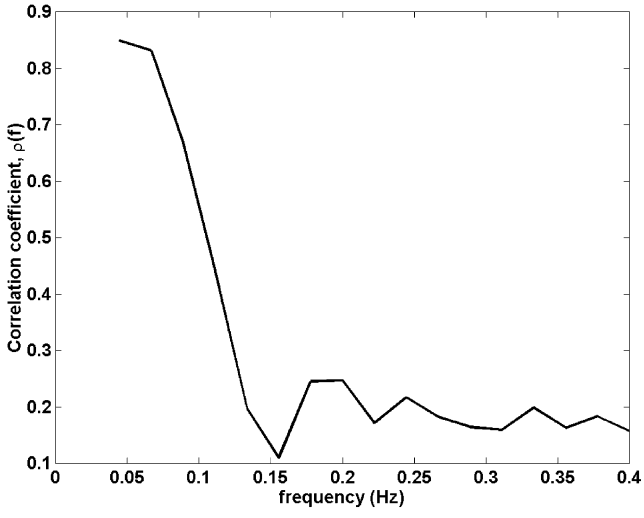

Fig. 7. Correlation between the wave spectrum at NDBC buoy 46026 and the power spectrum from the mudflat, between February 2 and 15. Good correlation is seen at low frequencies, with a value of $\rho(f) = 0.87$ at 0.044 Hz (22.5 s period) and $\rho(f) = 0.8$ at 0.067 Hz (15 s period). Frequencies larger than 0.15 Hz have a correlation of $\rho < 0.3$, indicating that the higher frequency signals are uncorrelated with the ocean wave spectrum.

(ocean waves) and from $\sim 10^{-4}$ to $\sim 10^{-2}$ $(m/s)^2$ for the high-frequency band (wind waves). In the frequency domain, we calculate a noise floor of order 0.002 $(m/s)^2$/Hz for the energy intensity calculations. Typical values of the energy intensity ranged between 0.005 and 0.05 $(m/s)^2$/Hz for the low-frequency band (ocean waves) and between 0.005 and 0.5 $(m/s)^2$/Hz for the high frequency band (wind waves), indicating a good signal to noise ratio (see Fig. 4). In practice, it appears that the error in the measured quantities may be significantly less than these estimates. Across the entire experiment, the spectra show a noise floor, that is less than $1.8 \times 10^{-6} \pm 1.3 \times 10^{-6}$ $(m/s)^2$. This results in a very conservative upper bound on the noise floor of 8×10^{-6} $(m/s)^2$, assuming a 3σ deviation from the average. This suggests that the theoretical values for the error in our calculated quantities are likely to be overestimates, and that the detected signals lie well above the noise levels.

Note that with a 45-s burst sampled at 10 Hz, we can resolve a spectrum of waves with frequencies below the Nyquist criterion of 5 Hz (e.g. Oppenheim & Schafer, 1989). At low frequencies, the frequency transformation cannot resolve waves with a periods longer than Δ, where Δ is the burst length; however, conventional wisdom holds that a period of $\Delta/2$, or 22.5 s, is the practical limit. Thus, both ocean waves (typically

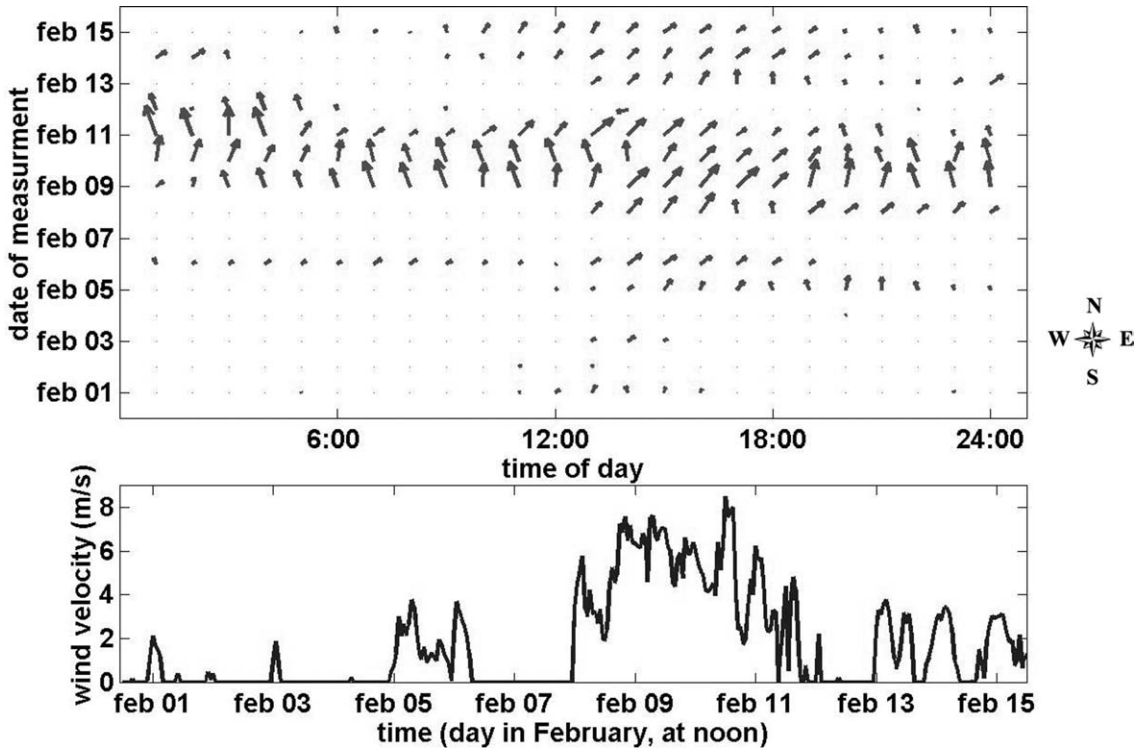

Fig. 8. Components of wind blowing unobstructed onto the mudflat from the south between 165° and 225° east of north. All other components of wind are set to zero. Note that the largest wind signal is seen during the storm of February 9–11, with a maximum wind speed of 8.5 m/s occurring early on February 11.

between 10 and 20 s periods) and local wind waves (defined in our analysis with periods between 1 and 5 s) are adequately characterized by our data set. Moreover, the high correlation seen between ocean waves and the low-frequency band of near-bed motions, as well as between wind energy and the high-frequency band, increases our confidence in the analysis.

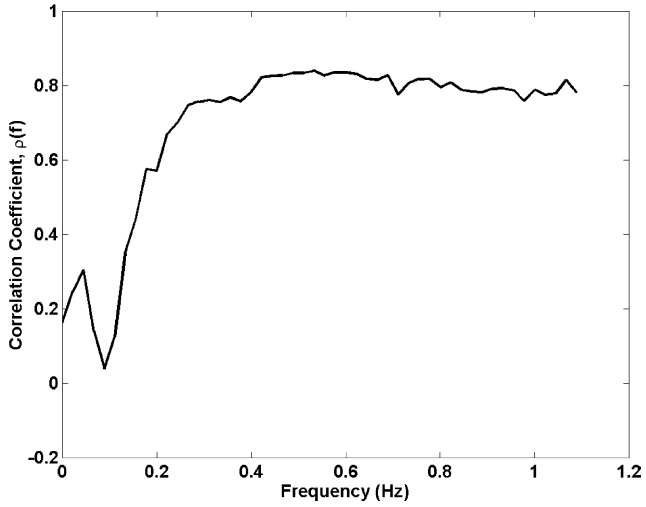

Fig. 9. Correlation of conditioned wind energy (wind velocity squared) with the tidally averaged power spectrum over the entire, two-week experimental period. At wave frequencies >0.25 Hz, the correlation coefficient $\rho(f) > 0.6$, indicating good correlation between wind and high frequency waves.

3.5. Calculation of bed stresses

The Reynolds stress acting in the near-bed region is most simply calculated using the covariance of the fluctuating vertical and horizontal components of velocity. Unless the waves are in perfect quadrature and the instrument is perfectly vertical, this method will include wave motions, and represent an aggregate of both wave and turbulent contributions. Waves can be filtered from stress estimates by a variety of methods, for example by subtracting velocity measurements from instruments spaced such that wave motions are correlated but turbulent fluctuations are uncorrelated (Shaw & Trowbridge, 2001; Trowbridge, 1998) or through the correlation of the currents with the pressure record to identify wave motions (Benilov & Filyuskin, 1970; Bowden & White, 1966; Wolf, 1999). With the data available (a single ADV and a loss of pressure data), unfortunately, neither of these methods is tenable for our analysis. Yet another method is to estimate turbulent shear stress based on the inertial subrange of the energy spectrum (Kolmogorov spectrum), accounting for waves theoretically (e.g. Gross, Williams, & Terray,

1994; Lumley & Terray, 1983). However, for measurements taken at a point, the inertial method requires that: (i) turbulent fluctuations are much less than the mean velocity (Taylor's frozen turbulence hypothesis), (ii) turbulence production balances dissipation, and (iii) a constant stress layer exists near the bed (Gross et al., 1994; Huntley, 1988; Wolf, 1999). Typically, only a small fraction of data in marine experiments satisfies these criteria (e.g. Wolf, 1999; Wright, Boon, Xu, & Kim, 1992). In our data set, few bursts reliably follow the $k^{-5/3}$ (k = wave number) decay of energy predicted by Kolmogorov.

Given the limitations of the environmental conditions and experimental data, and to avoid contamination by wave fluctuations, we calculated bed stress using the turbulent kinetic energy (TKE), following a modified form of the method suggested by Soulsby and Humphery (1989) and Soulsby (1983). Soulsby (1983) found that across a wide range of conditions, the bed shear stress in a marine boundary layer was given by $\tau_b = 0.19\rho q^2$, where q^2 is the TKE near the bed. Although similar to the dissipation method mentioned above, Soulsby (1983) argues that this method does not necessarily rely on the identification of a Kolmogorov spectrum in the inertial subrange. In our study, the depth of the flow provides a constraint on the development of the boundary layer. Instead of being bounded from above by uniform flow, the flow on this shallow mudflat is more likely to be approximated by open channel flow. In open channel flow, the TKE (q^2) decreases exponentially away from the bed (Nezu & Nakagawa, 1993)

$$q^2(z) = \overline{u_t^2} + \overline{v_t^2} + \overline{w_t^2} = 9.56u_*^2 \exp(-2z/H) \quad (4)$$

where $\overline{u_t^2}$, $\overline{v_t^2}$, and $\overline{w_t^2}$ are mean turbulent intensities in the horizontal and vertical directions, u_* is the friction velocity, and H is the depth of the water column. Using the definition of the friction velocity, we can convert this relationship into an expression for the bed stress

$$\tau_b = \rho u_*^2 = \rho(q^2/9.56)\exp(2z/H) \quad (5)$$

To estimate the TKE, we follow Soulsby and Humphery (1989), and linearly interpolate in log-space across the wind wave peaks, which extend from ~0.2 to ~1 Hz. Wind wave energy is removed, and the TKE is found by integrating the resulting energy spectrum from 0.15 to 2 Hz. Note that the upper limit denotes the approximate location of the noise floor, and the lower limit is placed at a frequency above the ocean swell spectrum. We placed the lower frequency limit above the ocean wave spectrum to be conservative, as there is low resolution at the lower frequencies, making interpolation across the ocean swell peak difficult. Thus, TKE is underestimated due to cut-off at both the high and low frequencies. However, the effect of the low-frequency cut-off is mitigated by the shallow depth, which restricts the length scale of turbulent eddies.

The results of this analysis are presented in Table 1 for three ebb tides with similar mean currents, but subject to different levels of wave forcing. The estimate of bed stress defined in Eq. (5) is given in the first column, and is normalized by the mean velocity squared (actually $\rho\bar{U}^2$) to define a drag coefficient in the final column. In case of no wave forcing, the implied drag coefficient is 0.0013, which is less than the typical value of 0.0025 for estuarine flows. This most likely occurs due to the underestimation of the TKE described above.

When more energetic waves are present, both the bed stress and the drag coefficient increase significantly, which is likely due to wave–current boundary layer interaction. As the ocean swell velocity scale (displayed as root mean square (rms) velocity in Table 1) increases from 3 to 5.5 cm/s, the drag coefficient increases by a factor of more than 4 to a value of 0.0061, approximately double the typically assumed estuarine value. If large local wind waves are also present (the last case in Table 2), the drag coefficient increases further to four times the typically assumed value (~0.01). Thus, both ocean swell and local wind waves can act to elevate the bed stress to values significantly above that typically assumed in estuarine models. Because ocean swell is a persistent signal (see Fig. 4), it is likely to be an important contributor to sediment dynamics at the site.

Table 1
Comparison of bed stress under conditions of (a) small waves and large ebb current (February 5, 2002), (b) significant ocean swell and ebb current (February 3, 2002), and (c) ocean swell, large wind waves, and ebb current (February 11, 2002)

	Bed stress τ_b (N/m^2)	Burst-averaged velocity $\bar{U}$ (cm/s)	rms ocean wave orbital velocity (cm/s)	rms wind wave orbital velocity (cm/s)	Drag coefficient $C_d = \tau_b/\rho\bar{U}^2$
(a) Small waves, large ebb current	0.04	17.35	3.16	2.00	0.0013
(b) Ocean swell, large ebb current	0.06	9.79	5.48	2.00	0.0061
(c) Wind waves, ocean swell, and large ebb current	0.14	11.44	5.29	16.00	0.0103

Bed stress was calculated using the open channel approximation of Nezu and Nakagawa (1993) and the TKE approximation method of Soulsby and Humphery (1989). The rms orbital velocity of ocean swell and wind waves, and TKE were found by partitioning the energy spectrum between the various components. Note the larger stress and drag coefficient as wave energy increases.

4. Discussion

The fact that ocean swells are, at certain times, an important contributor to the dynamics at this field site is surprising, given the geometry of the estuary and the orientation of the ocean swells. The inlet to the San Francisco Bay is a narrow strait oriented along a west–southwest/east–northeast axis. However, the direction of the dominant ocean swell at NDBC buoy 46042 in Monterey (approximately 150 km from NDBC buoy 46026) during the two-week experiment ranged between 300° and 320° east of true north (i.e. from the northwest). Thus, assuming that the directional spectrum at the Monterey buoy (46042) and the San Francisco buoy (46026) are comparable, the dominant swell approaches the inlet to San Francisco Bay at an angle greater than 45°. Referring to Fig. 1, the direct line of action of these waves as they enter the bay would be towards the San Francisco shoreline.

It is perhaps not surprising, however, that ocean swell undergoes extensive dispersion as it enters the bay, given the complex bathymetry of the region around the Golden Gate (including a deep channel (~100 m deep) at the inlet, a sill approximately 2 km east of the Golden Gate, several islands, and extensive tracts of shallow water (Fig. 1)). All these features will likely cause refraction, dispersion, and/or reflection of incoming waves, resulting in the spread of ocean wave energy to a large portion of the central bay coastline. What is perhaps more surprising is the fact that sufficient energy is retained in these waves for them to be significant to the hydrodynamics, once they reach the sheltered mudflat under consideration. Given the orientation of the incoming swell and the bathymetry of the bay, it is highly likely that intertidal mudflats around the rest of Central Bay, particularly south of Richmond, are subjected to larger ocean swell than our experimental site.

4.1. Relative importance of ocean swell

During the two weeks of the experiment, the mudflat was exposed to a full spring–neap cycle as well as extremes of calm and stormy weather. Fig. 10 shows how the dominant source of energy varies over a tide and between tides as hydrodynamic conditions change. In this figure, three different tidal periods are displayed (corresponding to morning and afternoon of February 7 (Fig. 10a and b) and the night of February 10 and 11 (Fig. 10c)), each with different energy characteristics. Total energy is divided into a tidal component (the burst-averaged mean), an ocean wave component (oscillations with periods between 9 and 22.5 s), and a wind wave component (oscillations with periods between 1 and 5 s). During large spring tides, when the local winds are calm, the tidal current dominates (Fig. 10b). By contrast, during stormy conditions, wind waves dominate, independent of the tidal conditions (Fig. 10c). During neap tides or, at a shorter timescale, during slack tides, ocean waves become an important energy source when local winds are calm (Fig. 10a).

Though ocean waves are important in the absence of other forcing, the action of wind and tidal currents clearly deliver more energy onto the mudflat. Table 2 shows that during the large tide at 12:00 am on February 11, for example, we measured an average wind energy of $\sim 0.0141\,(\mathrm{m/s})^2$ on the mudflat at frequencies between 0.2 and 1 Hz. By contrast, ocean waves sustained an average energy of only $0.0013\,(\mathrm{m/s})^2$ between 0.04 and 0.11 Hz during the maximum swell on February 2. However, as shown in Table 2, the lower limit of energy from ocean waves, wind waves, and tidal current are comparable, and suggest that a set of conditions can occur in which ocean waves dominate the energy spectrum.

Although ocean swell contributes to the hydrodynamic description of the shallow intertidal zone at our site, its role in sediment dynamics must be evaluated by considering the bed shear stresses. Though ocean waves averaged about 7% of the energy load over the two weeks of the experiment, with a range from 2 to 15%, the details of the implications for sediment transport are yet unclear. However, our analysis of bed stress suggests that bed stress is greatly increased by nonlinear interaction between ocean swell and the mean current (see Table 1). Thus, even small ocean swell may need to be considered when calculating energy dissipation. When bed stress due to local wind waves or current is near a critical threshold for erosion or deposition, even a small, added energy source such as ocean swell is important. In addition, though most ocean wave energy is dissipated in shallow bay waters, extreme values in the Rayleigh distribution bring episodic bursts of greater energy onto the mudflat (see Fig. 5). Thus, bed stress events due to ocean swell will occur episodically and will be much larger than the average bed stress.

It is important to note that considering just the bed stresses will almost certainly underestimate the importance of waves in the sediment dynamics. In particular,

Table 2
A comparison of the maximum and minimum average energy loads measured per tide for wind waves, ocean waves, and tidal currents from February 2 to 15, 2001

	Maximum ($(m/s)^2$)	Minimum ($(m/s)^2$)
Wind waves	0.0141	0.0002
Ocean waves	0.0013	0.0002
Current	0.0182	0.0006

Note that the average energy for wind waves and currents spans two orders of magnitude. Energy from an ocean wave is defined as the power spectrum between 0.04 and 0.11 Hz, while energy from wind waves is the power spectrum between 0.2 and 1 Hz. Current energy is measured as the square of mean velocity.

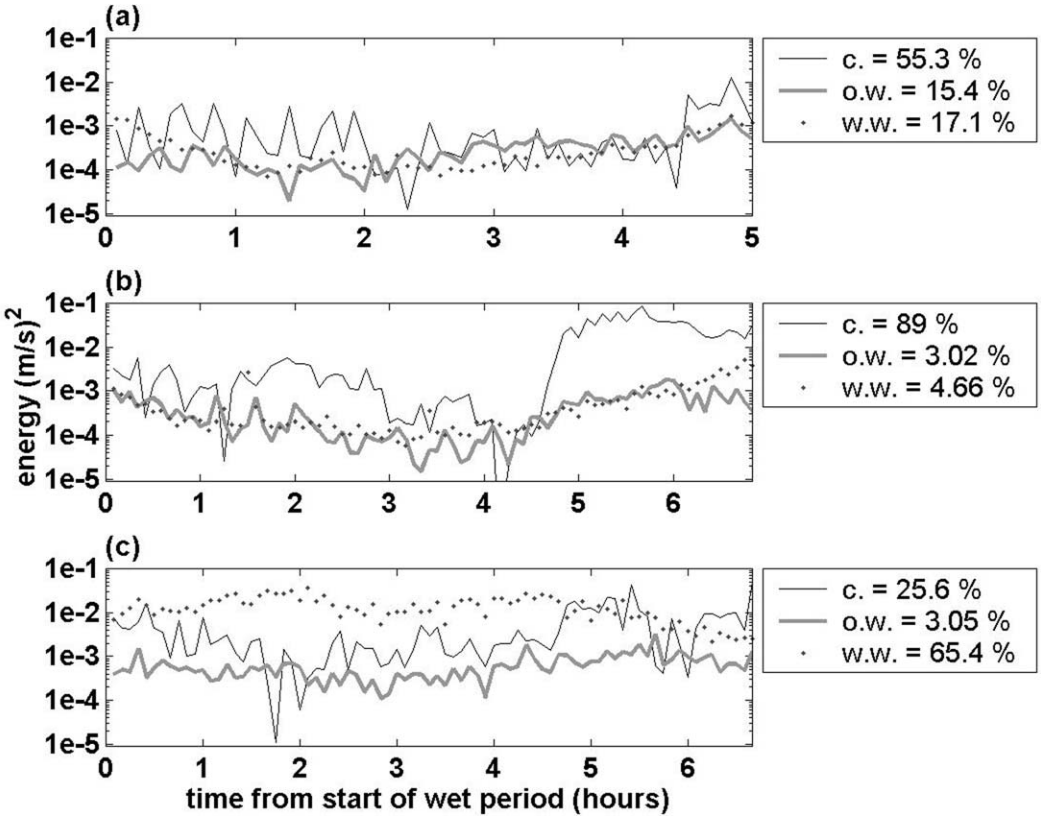

Fig. 10. Energy incident upon the mudflat over a wet period during low-energy conditions (a), current-dominated conditions (b), and wind-dominated conditions (c). The legend gives the percentage of energy coming from current (c.), ocean waves (o.w.), and wind waves (w.w.) for each tide. Wind waves are calculated from 0.2 to 1 Hz, ocean waves from 0.044 to 0.11 Hz. Note that the energy percentages do not equal unity, suggesting that there is some energy of other frequencies (e.g. low-frequency seiching or high-frequency wind waves and turbulence). (a) shows the small high tide occurring on February 7, and shows ocean waves becoming the largest energy source between 3 and 4.5 h. (b) shows the large high tide on February 7; note the large ebb current at the end of the tide. Finally, (c) shows wind wave dominated conditions during the storm of February 9–11.

the vertical acceleration and pressure fluctuations caused by waves at the bed can cause mud to fluidize and be transported in a mud layer (Li & Parchure, 1998; Wells & Kemp, 1986). Further, shear from currents, ocean waves, and wind waves not only interact with the bed on the mudflat through bed stresses, but play a role in both the aggregation and breakage of flocs (Van der Lee, 1998), thus modifying the depositional dynamics of cohesive sediments.

4.2. *Implications for sediment transport modeling*

Most sediment transport models apply hydrodynamic forcing and bed stress through either a current term or a combined wave–current formulation (see review by Fredsoe, 1993), where, for estuaries, the wave climate is estimated based on local wind forcing. Usually, the type of sediment transport model used depends on the individual characteristics of the study area. For example, in the Loire estuary, a sediment model using only tidal forcing found good agreement between the measured and simulated spatial distribution of the turbidity maximum and fluid mud (Le Normant, 2000). However, off channel waters and fringing mudflats may not be tidally dominated, which makes the time varying description of waves and currents important for determining sediment transport processes (Sanford, 1994). The nonlinear interaction between the wave boundary layer and currents creates an enhanced shear stress that is greater than the superposed stress from either waves or currents (see review by Soulsby et al., 1993). In estuaries with waves in differing frequency bands, the dominant frequency may vary in both space and time, and should be considered in models. For example, in the lower Chesapeake Bay at a depth of 10–12 m, wind waves generally dominated the wave spectrum, although a persistent, small amplitude ocean swell (~10 cm) dominated during calm, windless conditions (Wright et al., 1992). Similarly, a study in Cleveland Bay, Australia, found wave–current interaction due to both swell and wind waves, concluding that at depths of ~10–15 m, ocean waves were larger sources of stress than wind and tidal currents (Jing & Ridd, 1996). The results presented here from the San

Francisco Bay suggest that ocean swell can also be important in the interior of estuaries at very shallow depths, including waters in the intertidal zone.

Nonetheless, most hydrodynamic models of the shallower regions of semi-enclosed estuaries, such as the intertidal mudflats under consideration here, include only tidal and local wind forcing (e.g. Cheng, Casulli, & Gartner, 1993; Wood, Black, & Jago, 1998; Zhen-Gang, Morton, & Hamrick, 2000). However, ocean swell is by definition non-local, and large swell events may occur during otherwise calm periods (note the large swells of February 2 and 3 in Figs. 4 and 6). Furthermore, ocean swell adds a small amount of energy to the total energy budget even during large local events, and is thus a source of error in current sediment models. The influence of ocean swells will not be uniform, however, and the propagation of swells into the estuary, including their refraction and reflection by the local bathymetry, must be considered. To address this complexity, we would argue that a complete model of sediment dynamics in semi-enclosed coastal estuaries should include both a wave propagation model to bring ocean swell into the estuary (e.g. SWAN, see review by Booij, Ris, & Holthuijsen, 1999) and a traditional estuarine circulation model (with tidal and local wind forcing) to define the local sediment transport that results.

5. Summary and conclusions

The two weeks of high-resolution velocity measurements in the intertidal zone of a semi-enclosed estuary have suggested that ocean swell is important for the energy of the flows and potentially the shear stress in this environment. While local wind forcing dominates such considerations when the orientation of the wind is directed onto the mudflat, when local wind forcing is limited—which is likely to be the case on many sheltered mudflats, or during certain seasons—ocean swell becomes an important constituent in the dynamics of these very shallow regions that fringe many estuaries.

In general, the effects of ocean swell along the margins of an estuary have not been considered in the current generation of numerical models of estuaries. It is likely that the non-local dynamics of ocean swell will also be relevant in models of estuarine sediment transport, in particular areas such as the central San Francisco Bay, and during episodic swell events in the winter season.

Acknowledgements

The authors thank David Ralston, Jon Fram, and Deanna Sereno for logistical support during the experiment. This research was funded by National Institutes of Health grant P42ES0475 from the National Institute of Environmental Health Sciences.

References

Bendat, J. S., & Piersol, A. G. (1966). *Measurement and analysis of random data*. New York: Wiley.

Benilov, A. Y., & Filyuskin, B. N. (1970). Application of methods of linear filtration to an analysis of fluctuations in the surface layer of the sea. *Izvestiya. Atmospheric and Oceanic Physics 6*, 810–819.

Booij, N., Ris, C., & Holthuijsen, L. H. (1999). A third generation wave model for coastal regions. 1. Model description and validation. *Journal of Geophysical Research 104*, 7649–7666.

Bowden, K. F., & White, R. A. (1966). Measurement of the orbital velocities of sea waves and use in determining the directional spectrum. *Geophysical Journal 12*, 1.

Cheng, R. T., Casulli, V., & Gartner, J. W. (1993). Tidal, residual and intertidal mudflat (TRIM) model and its applications to San Francisco Bay, California. *Estuarine, Coastal and Shelf Science 36*, 235–280.

Christie, M. C., & Dyer, K. R. (1998). Measurements of the turbid tidal edge over the Skeffling mudflats. In K. S. Black, D. M. Patterson, & A. Cramp (Eds.), *Sedimentary processes in the intertidal zone*, *Special publications, 139* (pp. 45–55). London: Geological Society.

De Lange, W., & Healy, T. (1990). Wave spectra for a shallow mesotidal estuarine lagoon: Bay of Plenty, New Zealand. *Journal of Coastal Research 6*(1), 189–199.

Dyer, K. R. (1989). Sediment processes in estuaries: future research requirements. *Journal of Geophysical Research 194*(C10), 14327–14339.

Dyer, K. R. (1998). The typology of intertidal mudflats. In K. S. Black, D. M. Patterson, & A. Cramp (Eds.), *Sedimentary processes in the intertidal zone*, *Special publications, 139* (pp. 11–24). London: Geological Society.

Fredsoe, J. (1993). Modelling of non-cohesive sediment transport processes in the marine environment. *Coastal Engineering 21*, 71–103.

Grant, W. D., & Madsen, O. S. (1979). Combined wave and current interaction with a rough bottom. *Journal of Geophysical Research 84*(C4), 1797–1808.

Green, M. O., & MacDonald, I. T. (2001). Processes driving estuary infilling by marine sands on an embayed coast. *Marine Geology 178*, 11–37.

Gross, T. F., Williams, A. J., & Terray, E. A. (1994). Bottom boundary layer spectral dissipation estimates in the presence of wave motions. *Continental Shelf Research 14*(10/11), 1239–1256.

Horne, A. J., & Goldman, C. R. (1994). *Limnology*. McGraw-Hill, New York.

Huntley, D. A. (1988). A modified inertial dissipation method for estimating seabed stresses at low Reynolds numbers, with application to wave/current boundary layer measurements. *Journal of Physical Oceanography 18*, 339–346.

Janssen-Stelder, B. (2000). The effect of different hydrodynamic conditions on the morphodynamics of a tidal mudflat in the Dutch Wadden Sea. *Continental Shelf Research 20*, 1461–1478.

Jing, L., & Ridd, P. V. (1996). Wave–current bottom shear stresses and sediment resuspension in Cleveland Bay, Australia. *Coastal Engineering 29*, 169–186.

Krone, R. B. (1962). *Flume studies of the transport of sediments in estuarial shoaling processes*. Final report. Hydraulic Engineering Laboratory and Sanitary Engineering Research Laboratory, University of California, Berkeley.

Li, Y., & Parchure, T. M. (1998). Mudbanks of the southwest coast of India. VI: Suspended sediment profiles. *Journal of Coastal Research 14*(4), 1363–1372.

Le Normant, C. (2000). Three-dimensional modeling of cohesive sediment transport in the Loire estuary. *Hydrological Processes 14*, 2231–2243.

Longuet-Higgins, M. S. (1952). On statistical distribution of the heights of sea waves. *Journal of Marine Research 11*, 245–266.

Lumley, J. L., & Terray, E. A. (1983). Kinematics of turbulence convected by a random wave field. *Journal of Physical Oceanography 13*, 2000–2007.

Nezu, I., & Nakagawa, H. (1993). *Turbulence in open channel flows, International association for hydraulic research. Monograph series*. Rotterdam: Balkema.

Oppenheim, A. V., & Schafer, R. W. (1989). *Discrete time signal processing*. Englewood Cliffs: Prentice-Hall.

Partheniades, E. (1962). *A study of erosion and deposition of cohesive soils in salt water* (182 pp.). PhD thesis, University of California at Berkeley.

Sanford, L. P. (1994). Wave-forced resuspension of upper Chesapeake Bay muds. *Estuaries 17*(18), 148–165.

Shanmugan, K., & Breiphol, A. M. (1998). *Random signals: Detection, estimation, and data analysis*. New York: Wiley.

Shaw, W. J., & Trowbridge, J. H. (2001). The direct estimation of near-bottom turbulent fluxes in the presence of energetic wave motions. *Journal of Atmospheric and Oceanic Technology 18*, 1540–1557.

Shi, N. C., & Larsen, L. H. (1984). Reverse sediment transport induced by amplitude-modulated waves. *Marine Geology 54*, 181–200.

SonTek ADV acoustic Doppler velocimeter, technical documentation (2001). San Diego: SonTex Inc.

Soulsby, R. L. (1983). The bottom boundary layer of shelf seas. In B. Johns (Ed.), *Physical oceanography of coastal and shelf seas* (pp. 189–266). Amsterdam: Elsevier.

Soulsby, R. L., Hamm, L., Klopman, G., Myrhaug, D., Simons, R. R., & Thomas, G. P. (1993). Wave–current interaction within and outside the bottom boundary layer. *Coastal Engineering 21*, 41–69.

Soulsby, R. L., & Humphery, J. D. (1989). Field observations of wave–current interaction at the sea bed. In A. Torum, & O. T. Gudmestad (Eds.), *Proceedings of NATO advanced research workshop on water wave kinematics, Molde, Norway, 22–25 May 1989* (pp. 413–428). Dordrecht: Kluwer Academic.

Trowbridge, J. H. (1998). On a technique for measurement of turbulent shear stress in the presence of surface waves. *Journal of Atmospheric and Oceanic Technology 15*, 290–298.

Van der Lee, W. T. B. (1998). The impact of fluid shear and the suspended sediment concentration on the mud floc size variation in the Dollard estuary, The Netherlands. In K. S. Black, D. M. Patterson, & A. Cramp (Eds.), *Sedimentary processes in the intertidal zone*, *Special publications, 139* (pp. 187–198). London: Geological Society.

Wells, J. T., & Kemp, P. G. (1986). Interaction of surface waves and cohesive sediments: field observations and geologic significance. In A. J. Mehta (Ed.), *Estuarine cohesive sediment dynamics, lecture notes on coastal and estuarine studies no. 14* (pp. 43–65). Berlin: Springer.

Whitehouse, R. J. S., & Mitchener, H. J. (1998). Observations of the morphodynamic behavior of an intertidal mudflat at different timescales. In K. S. Black, D. M. Patterson, & A. Cramp (Eds.), *Sedimentary processes in the intertidal zone*, *Special publications, 139* (pp. 255–271). London: Geological Society.

Widdows, J., Brinsley, M., & Elliott, M. (1998). Use of in-situ flume to quantify particle flux (biodeposition rates and sediment erosion) for an intertidal mudflat in relation to changes in current velocity and benthic macrofauna. In K. S. Black, D. M. Patterson, & A. Cramp (Eds.), *Sedimentary processes in the intertidal zone*, *Special publications, 139* (pp. 85–97). London: Geological Society.

Wolf, J. (1999). The estimation of shear stresses from near-bed turbulent velocities for combined wave–current flows. *Coastal Engineering 37*, 529–543.

Wood, R. G., Black, K. S., & Jago, C. F. (1998). Measurements of preliminary modeling of current velocity over an intertidal mudflat, Humber estuary, UK. In K. S. Black, D. M. Patterson, & A. Cramp (Eds.), *Sedimentary processes in the intertidal zone*, *Special publications, 139* (pp. 167–175). London: Geological Society.

Wright, L. D., Boon, J. D., Xu, J. P., & Kim, S. C. (1992). The bottom boundary layer of the Bay Stem Plains environment of lower Chesapeake Bay. *Estuarine, Coastal and Shelf Science 35*, 17–36.

Zhen-Gang, J., Morton, M. R., & Hamrick, J. M. (2000). Modeling hydrodynamic and sediment processes in Morro Bay. In M. L. Spaulding, & H. L. Butler (Eds.), *Estuarine and coastal modeling; proceedings of the sixth international conference Vol. 6* (pp. 1035–1054).